

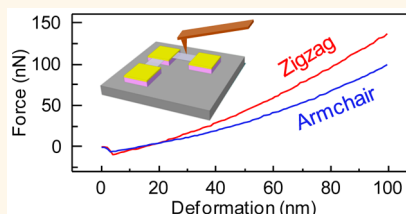
# Mechanical and Electrical Anisotropy of Few-Layer Black Phosphorus

Jin Tao,<sup>†</sup> Wanfu Shen,<sup>†</sup> Sen Wu,<sup>\*,†</sup> Lu Liu,<sup>†</sup> Zhihong Feng,<sup>†</sup> Chao Wang,<sup>†</sup> Chunguang Hu,<sup>†</sup> Pei Yao,<sup>‡</sup> Hao Zhang,<sup>†</sup> Wei Pang,<sup>†</sup> Xuexin Duan,<sup>†</sup> Jing Liu,<sup>†</sup> Chongwu Zhou,<sup>§</sup> and Daihua Zhang<sup>\*,†</sup>

<sup>†</sup>State Key Laboratory of Precision Measuring Technology & Instruments, College of Precision Instrument and Optoelectronics Engineering, and

<sup>‡</sup>Center for Analysis and Tests, Tianjin University, Tianjin 300072, China and <sup>§</sup>Department of Electrical Engineering, University of Southern California, Los Angeles, California 90089, United States

**ABSTRACT** We combined reflection difference microscopy, electron transport measurements, and atomic force microscopy to characterize the mechanical and electrical anisotropy of few-layer black phosphorus. We were able to identify the lattice orientations of the two-dimensional material and construct suspended structures aligned with specific crystal axes. The approach allowed us to probe the anisotropic mechanical and electrical properties along each lattice axis in separate measurements. We measured the Young's modulus of few-layer black phosphorus to be  $58.6 \pm 11.7$  and  $27.2 \pm 4.1$  GPa in zigzag and armchair directions. The breaking stress scaled almost linearly with the Young's modulus and was measured to be  $4.79 \pm 1.43$  and  $2.31 \pm 0.71$  GPa in the two directions. We have also observed highly anisotropic transport behavior in black phosphorus and derived the conductance anisotropy to be 63.7%. The test results agreed well with theoretical predictions. Our work provided very valuable experimental data and suggested an effective characterization means for future studies on black phosphorus and anisotropic two-dimensional nanomaterials in general.



**KEYWORDS:** black phosphorus · reflection difference microscopy · plasma trim · AFM bending · anisotropic conductance · anisotropic Young's modulus · breaking stress and strain

Few-layer black phosphorus (BP) has drawn increasing interest over the past years due to its unique and superior electrical and optical properties.<sup>1–7</sup> BP film is an outstanding semiconductor and delivers excellent room-temperature carrier mobility and on/off ratio at the same time when configured into field effect transistors (FETs).<sup>4–6,8,9</sup> On the other hand, the thickness-dependent band structure of BP makes it an appealing candidate material for tunable photodetection across a wide spectrum from visible to infrared light.<sup>10–13</sup>

Besides the electrical and optical properties, the mechanical attributes of two-dimensional (2D) nanomaterials are of great importance as well. Extensive studies have focused on the mechanical, piezo-electrical, and piezo-resistive characteristics of graphene<sup>14–16</sup> and MoS<sub>2</sub> films.<sup>17–20</sup> These 2D materials demonstrated great potential in a wide range of applications including flexible electronics, strain sensors, electro-mechanical resonators, and even nanoscale generators based on piezoelectricity.<sup>19,21–23</sup> At the same time, the mechanical behaviors of 2D materials reveal a wealth of physics and provide

valuable insights into the lattice–electron interactions in low-dimensional systems. Taking BP as an example, theoretical studies predicted that in-plane strains in monolayer BP could substantially modify its electronic band structure, resulting in dramatic and anisotropic change in carrier mobility along zigzag and armchair directions.<sup>24–27</sup> In another theoretical work, researchers discovered negative Poisson's ratio in single-layer BP when a uniaxial stress along the zigzag direction is applied.<sup>28</sup> These unique electron transport and mechanical behaviors are valuable for both scientific studies such as unusual quantum Hall effects and exploration of exotic mechanical and electronic applications.

In contrast to a large number of investigations on graphene<sup>14,15</sup> and MoS<sub>2</sub>,<sup>17,18</sup> few have focused on the mechanical properties of BP despite limited theoretical studies.<sup>29–31</sup> Calculations based on first-principles theory revealed anisotropic Young's moduli along zigzag and armchair directions, with a ratio of approximately 2.5 in single- and few-layer BP films.<sup>31</sup> This large anisotropy ratio is very rare among 2D and bulk materials. An experimental verification

\* Address correspondence to senwu@tju.edu.cn, dhzhang@tju.edu.cn.

Received for review August 18, 2015 and accepted September 30, 2015.

Published online 10.1021/acsnano.5b05151

© XXXX American Chemical Society

would be of great interest. However, the measurement is nontrivial, as the setup has to differentiate and decouple signals from two orthogonal lattice directions. Standard characterization means by suspending 2D films on circular cavities<sup>14,17</sup> is not directly applicable in this case because of the symmetric arrangement.

To meet this specific challenge, we have developed a series of fabrication and characterization techniques. The first step involved an innovative approach, reflectance difference microscopy (RDM), to identify the crystal orientations of individual BP flakes on a Si/SiO<sub>2</sub> substrate. Compared to high-resolution transmission electron microscopy (HRTEM) and polarization-resolved Raman spectroscopy, RDM provides the most rapid and direct visualization of the lattice orientations in an *in situ* and nondestructive manner. In the second step, we trimmed each BP flake with Ar<sup>+</sup> plasma and shaped it into two strips that are separately aligned with the armchair and zigzag axes. This was followed by anchor/electrode formation at the ends of the strips and subsequent sacrificial layer (SiO<sub>2</sub>) release to suspend the structure. This key step allowed us to probe the mechanical and electrical properties of BP strips perfectly aligned with the principal lattice axes, thereby minimizing signal mixing from different orientations. In the last step, we used atomic force microscopy (AFM) to characterize the anisotropic mechanical properties of the BP samples. Our test results revealed anisotropic Young's moduli with a ratio of  $2.21 \pm 0.67$  between the zigzag and armchair directions, which was in good accordance with previous theoretical predictions. We have also successfully measured the anisotropic breaking stress of the BP film, which gave distinct values in the two directions with a ratio comparable to that of the Young's modulus. This has resulted in nearly isotropic breaking strain according to our derivation. The value varied from 5.3% to 9.2% in different samples, in a similar range to that observed in graphene and MoS<sub>2</sub> membranes.<sup>14,18</sup>

## RESULTS AND DISCUSSION

**Lattice Orientation Identification by RDM.** RDM measures the difference in reflectance of normal incidence plane polarized light between orthogonal directions in the surface plane normalized to the mean reflectance:<sup>32–34</sup>

$$\frac{\Delta r}{r} = \frac{2(r_x - r_y)}{r_x + r_y} \quad (1)$$

where  $x$  and  $y$  are internal reference orientations of the microscope. When we vary the relative orientations ( $\theta$ ) between the RDM and an orthorhombic crystal, the measurement renders a dimensionless value  $N(\theta)$  that periodically changes with  $\theta$  in the following way:

$$N(\theta) = \frac{2(r_{\parallel} - r_{\perp})}{r_{\parallel} + r_{\perp}} \cos(2\theta) \quad (2)$$

where  $r_{\parallel}$  and  $r_{\perp}$  are the reflectance in the two principal lattice directions of the orthorhombic crystal.

On a perfectly isotropic crystal,  $N(\theta)$  is zero for all angles. For anisotropic samples such as BP,  $N(\theta)$  reaches a maximum or minimum value when the orientation of RDM matches the armchair or zigzag direction. The technique can therefore be used to evaluate the anisotropic level of given crystal lattices and, more importantly, to identify the directions of principal axes.

Figure 1a and b demonstrate a typical RDM measurement. We first located a BP flake on a Si/SiO<sub>2</sub> wafer under an optical microscope, then recorded  $N(\theta)$  while rotating the incident polarization from  $\theta = 0^\circ$  to  $360^\circ$ . The polar plot of Figure 1b shows the absolute values of  $N$  taken at the center of the sample as a function of  $\theta$ , where we can identify the two high-symmetry axes located at  $50^\circ$  and  $140^\circ$ , respectively.

RDM serves as an imaging tool as well, which is able to simultaneously collect  $N(\theta)$  at all pixels inside the entire field of view and create a direct visualization of the anisotropy contrast. Figure 1c shows the RDM images taken at different angles with  $N(\theta)$  plotted in color scale. The reflection difference on the BP flake reached a maximum and minimum at the two orthogonal high-symmetry axes, respectively, while signals from the isotropic background were nearly zero. For polycrystalline samples with multiple lattice domains, RDM can also serve as a powerful and convenient tool to visualize the spatial distribution of lattice orientations. We have carried out systematic studies using RDM to characterize the anisotropy and domain distribution of a rich set of 2D materials. The results will be discussed in a separate report.

Long-time exposure to ambient conditions would degrade thin BP flakes gradually.<sup>35–37</sup> To minimize the exposure of BP flakes, we reduced the angular range to  $\theta = 0–90^\circ$  in a typical measurement and took seven data points with a resolution of  $15^\circ$ . The adjustment allowed us to complete the entire scan within 15 min for each sample. We then used sine fitting to determine the lattice orientations. The AFM image of the BP flake used in a typical test (14.8 nm in thickness) and its fitted RDM curve are shown in Figure 1d and e. It is important to note that even if we can identify the orientations of the two principal lattice axes, we are not able to assign them to specific axes, *i.e.*, zigzag or armchair, at this point. The reflection difference between two orthogonal polarization angles results from complex interactions between the incident photon and the electronic bands in the crystal.<sup>38,39</sup> A deterministic correlation between the  $N$  values and specific lattice orientations is still lacking. We then took an alternative approach in the following study and utilized electron transport measurements to distinguish zigzag vs armchair directions. A detailed analysis will be discussed in a later section.

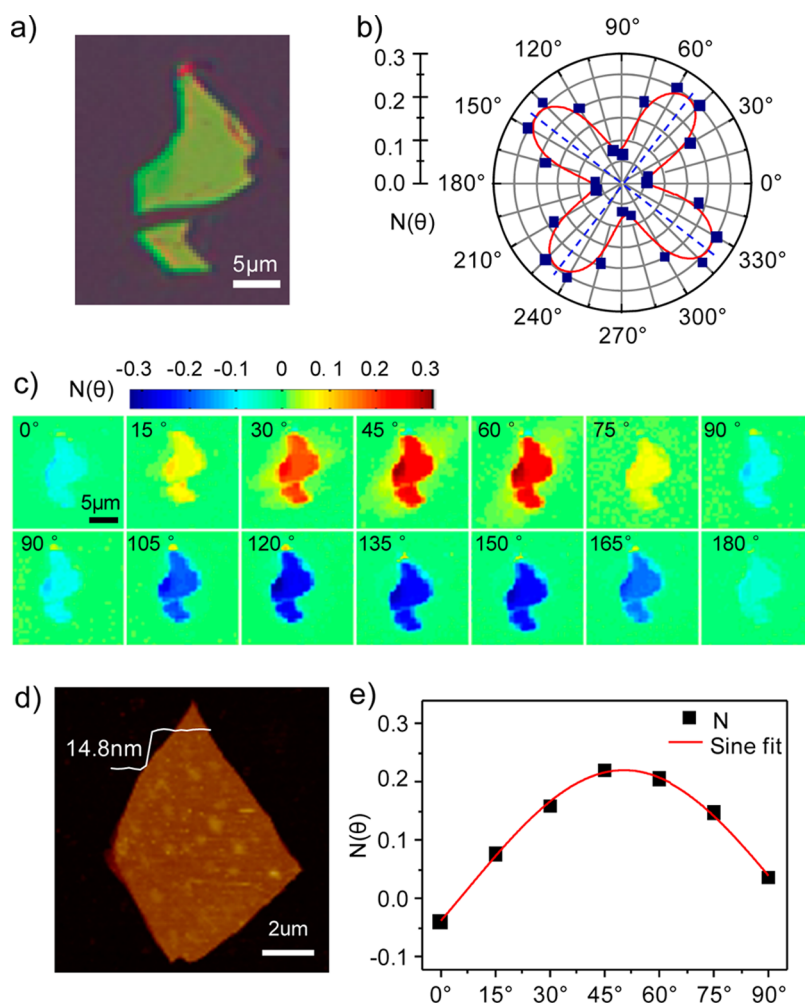


**Figure 1.** Identification of lattice orientation of a BP flake by RDM. (a) Optical image of the thin BP flake transferred onto a Si/SiO<sub>2</sub> substrate by mechanical exfoliation. (b) RDM results of the same BP flake (a) in polar coordinates. (c) RDM images taken at different angles. (d) AFM image of a typical BP flake used in the following electrical and mechanical measurements. Small bumps were occasionally visible on the surface of the flake due to material degradation in the ambient environment. (e) RDM signals of the BP flake shown in (d).

**Fabrication of Suspended BP Strips.** With the RDM results we were able to shape BP flakes into strips along the two principal lattice axes. The process flow is shown in Figure 2. First, few-layer BP flakes were transferred onto a Si/SiO<sub>2</sub> substrate by mechanical exfoliation from a bulk BP crystal. The thickness of the BP flakes, as measured by AFM, ranged from 14 to 28 nm in our experiment. We then performed electron beam lithography (EBL) with a negative e-beam resist to pattern an L shape on each sample, with the arms aligned with the two principal axes of BP separately. This was followed by Ar<sup>+</sup> plasma trimming and e-beam resist removal to transfer the pattern to the BP flake, as shown in Figure 2b and c. The Ar<sup>+</sup> trimming recipe was optimized to give a gentle and slow etch rate to minimize substrate overetch and prevent BP curving near the edges. Overetching into the substrate may cause peeling of the metal electrodes (to be deposited in the next fabrication step) upon sacrificial layer (SiO<sub>2</sub>) release and damage the suspended structure.

Curved edges of the BP strip would induce internal stress and modulate the stiffness of the suspended beam in an uncontrolled manner. The trimming recipe was eventually optimized as follows: Ar flow = 80 sccm; pressure = 20 Pa; RF power = 80 W. The trimming rate was approximately 0.5 nm/s. The trimming time varied for different samples depending on the thickness measured by AFM.

Figure 2d depicts the process of metal electrode formation and sacrificial layer release. Three metal electrodes (Cr/Au ≈ 8/80 nm) were patterned and deposited at the ends of the strips by the electron-beam evaporation and lift-off process. The electrodes formed electrical connections of the BP strips with external test circuits and served as mechanical anchors to hold the suspended structure at the same time. We then immersed the samples into BOE (ammonia/hydrofluoric acid = 7:1) for 3 min to release the SiO<sub>2</sub> sacrificial layer. The samples were then cleaned with deionized water. Special care should be taken when

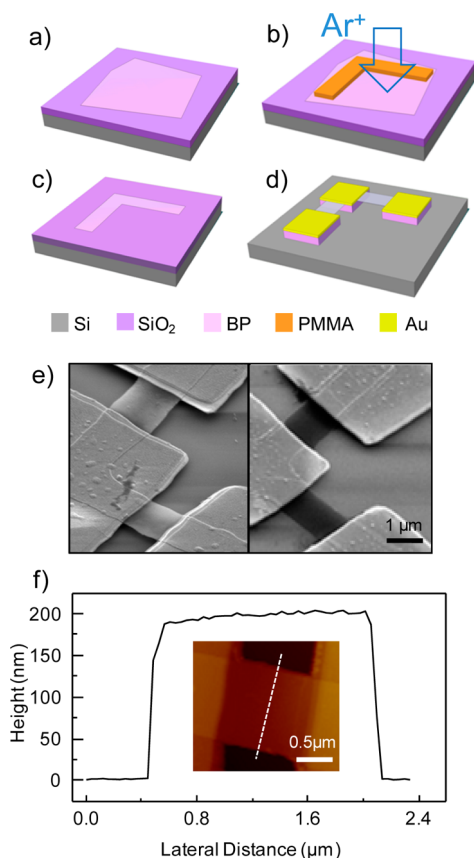


**Figure 2.** Fabrication process of suspended BP strips. (a) A BP flake was transferred onto a Si/SiO<sub>2</sub> substrate. RDM measurement was then used to identify the lattice orientations of the flake. (b) A layer of PMMA was spin-coated and then patterned by EBL into an L shape, with each arm aligned with a principal lattice axis, respectively. (c) The L-shaped pattern was then transferred to the BP flake after Ar<sup>+</sup> plasma etching and PMMA removal. (d) Metal electrode formation at the end of each strip and sacrificial layer release in BOE solution. (e) SEM image of a pair of successfully suspended BP strips (left) and collapsed strips damaged during drying due to high surface tension of water (right). (f) AFM image of a suspended BP strip and topology profile scanned across the dashed line marked in the inset.

drying the samples as the surface tension of water could easily collapse the suspended BP beams. Hexane could be used to dry the samples due to its lower surface tension,<sup>40</sup> but resulted in a low device yield. We adopted a critical point dryer with liquid CO<sub>2</sub> in our experiment to achieve a much higher yield.<sup>41</sup> Figure 2e (left) shows the SEM image of a pair of successfully released BP strips, as compared to the collapsed strips shown in the right image.

Figure 2f is the AFM measurement performed on a suspended device. The trench depth between the two metal electrodes is primarily determined by the thickness of the sacrificial layer and measured to be ~200 nm from the top surface of the BP to the trench bottom. To confirm the SiO<sub>2</sub> beneath the BP film was fully removed, we repeated the AFM measurement after peeling off the suspended BP and observed a perfectly flat surface along the bottom of the trench.

**Anisotropic Electron Transport Behaviors.** The transport behavior provides crucial information to our investigations on the mechanical anisotropy of BP. First, there has existed a library of experimental data on the transport properties of few-layer BP,<sup>5,27,42</sup> which helps us to cross-reference the previous work and evaluate the quality of our material and processes. Second, as discussed in the RDM section, we are lacking an established theory to definitively correlate the peak positions in an RDM curve to specific lattice directions. The electron transport characterization provides an alternative approach to distinguish the two high-symmetry axes, zigzag and armchair, from each other.

The atomic structure of monolayer BP is highly anisotropic. The band dispersion and effective mass of charge carriers are different along different crystal-line orientations, leading to anisotropic conductance in monolayer BP.<sup>27</sup> Few-layer BP has similar anisotropic properties. Theoretical simulations revealed that both the electron and hole mobilities are significantly higher along the armchair direction than that along the zigzag by a factor of approximately 1.5 to 3, indicating higher conductance in the armchair direction.<sup>42</sup>

The theoretical analysis in previous works allowed us to distinguish each BP strip in the pair from each other. Figure 3a presents the *I*–*V* measurements on the device shown in the inset SEM image. Both BP strips (labeled as DS<sub>1</sub> and DS<sub>2</sub>) were negatively biased at  $V_{GS} = -40$  V by the bottom gate. From the linear *I*–*V* curves we derived the conductance of DS<sub>1</sub> and DS<sub>2</sub> to be 7.54 and 14.58 μS, respectively. This corresponds to a conductance anisotropy (defined as  $(G_x - G_y)/[(G_x + G_y)/2]$ ,  $G_x$  and  $G_y$  are the conductance along the two orthogonal directions) of ~63.7%, in good agreement with the reported data.<sup>6</sup> The two BP strips, DS<sub>1</sub> and DS<sub>2</sub>, are presumably aligned with the zigzag and armchair directions, respectively, in this specific case.

Figure 3b shows the transfer characteristics of the two BP devices at  $V_{DS} = 50$  mV. The inset plots the same set of data in logarithm scale. Both devices are p-type within the scanning range of gate bias from –40 to 40 V. The hole mobilities were estimated to be 247 and 392 cm<sup>2</sup>/(V s) for DS<sub>1</sub> (zigzag) and DS<sub>2</sub> (armchair), respectively, and the on–off ratio was on the order of 10<sup>4</sup> to 10<sup>5</sup> in both devices. The conductance anisotropy varied between 30% and 130% at different gate bias below the threshold voltage  $V_{GS} = -15$  V. In Figure 3c, we recorded *I*–*V* curves at different gate bias for both devices. The linear and symmetric curves indicated good metallic contact at the BP and Cr/Au interface.

**Anisotropic Young's Modulus.** The suspended strips aligned in the armchair and zigzag directions allow us to carry out systematic measurements of the anisotropic Young's modulus of few-layer BP. We adopted the AFM bending method as described in a number of previous reports.<sup>14,15,43</sup> To minimize damage to the BP strips, the AFM was first operated in tapping mode for

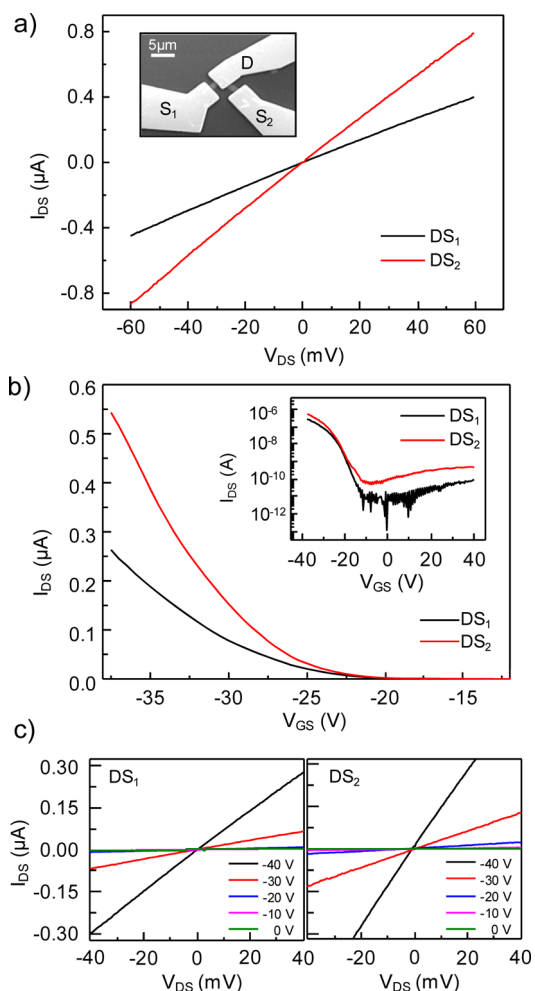


**Figure 3.** Anisotropic transport behaviors of BP. (a)  $I$ – $V$  curves of two orthogonal BP strips at  $V_{GS} = -40$  V. The inset shows the SEM image of the same device. The conductance anisotropy was calculated to be 63.7% according to the results. (b) Transfer characteristics of the two BP strips at  $V_{DS} = 50$  mV, from which we could derive the carrier mobilities as 392 and 247  $cm^2/(V s)$  in the armchair and zigzag directions, respectively. The inset curves are plotted in logarithm scale. (c) Output characteristics showing linear  $I$ – $V$  and anisotropic conductance at different gate bias.

imaging to determine the geometric dimension of the sample. In our experiments, the length of the BP strips ranged from 0.80 to 1.92  $\mu m$ , and the width ranged from 0.48 to 1.47  $\mu m$ . To achieve good accuracy of the bending test, the spring constant of the AFM cantilever must be very close to the stiffness of the BP strip at the loading point.<sup>15</sup> According to the estimation by the finite element method (FEM) (assuming the Young's modulus of BP is 41 GPa/106 GPa in the armchair/zigzag direction<sup>31</sup>), the stiffness (in small deflection) at the midpoint of the suspended BP strips is in the range 1–5 N/m. Thus, we chose the AFM cantilevers with the nominal spring constant of 3 N/m for the bending tests. Since the nominal spring constant may have large uncertainty due to limitations of the current manufacturing technique, we calibrated the AFM cantilever using a traceable method before each test,<sup>44</sup>

and the calibrated effective spring constants were used instead of the nominal values for Young's modulus calculations.

Figure 4a shows the schematic of the bending test. The AFM cantilever tip was placed at the center of the suspended BP strip first and then moved 100 nm downward and upward with a speed of 0.5  $\mu m/s$  to bend and release the BP strip. The vertical deformation of BP,  $\delta_{BP}$ , can be derived by

$$\delta_{BP} = \Delta z - D_{cant} \quad (3)$$

where  $\Delta z$  is the vertical displacement of the AFM cantilever, which is given by the displacement sensor of the Z-scanner, and  $D_{cant}$  is the cantilever deflection, which is detected by the photodiode of the AFM system. The loading force can be written as  $F = k_{cant}D_{cant}$ , where  $k_{cant}$  is the effective spring constant of the AFM cantilever.

We assumed that the BP strips were firmly fixed by the metal electrodes at the two ends. The mechanical configuration can therefore be simplified as a clamped–clamped beam with a concentrated force load at the midpoint in this case. The following equation correlates the loading force  $F$  and the beam deflection  $\delta_{BP}$ .<sup>15,43</sup>

$$F = \frac{\pi^4 Ewt^3}{6L^3} \delta_{BP} + \frac{\pi^4 Ewt}{8L^3} \delta_{BP}^3 + \frac{T}{L} \delta_{BP} \quad (4)$$

where  $E$  is the Young's modulus of BP;  $w$ ,  $L$ , and  $t$  are the width, length, and thickness of the strip, respectively; and  $T$  is the pretension in the suspended film. The first term in eq 3 corresponds to linear elastic response due to bending. The second term represents nonlinear elastic response under large deformation due to stretching, and the last term takes into account the pretension in the beam. The finite length-to-width ratio of the beam and anisotropic material properties will affect the accuracy of eq 4. Timoshenko *et al.* have provided very comprehensive discussions regarding the errors and corrections.<sup>45</sup>

Figure 4b shows the typical force–deflection curves of a pair of orthogonal strips trimmed from the same BP flake. The two beams exhibited different elastic response due to the anisotropic Young's modulus. The inset shows a zoom-in plot of the initial part of the force curve. The beam deflection increased linearly with the loading force in the first 6 nm and became nonlinear at larger deflections.

At small deflections, the stiffness at the midpoint of the suspended BP beams, namely, the ratio of loading force vs the beam deflection, is given by the following equation:

$$k_{BP} = \frac{\pi^4 Ewt^3}{6L^3} + \frac{T}{L} \quad (5)$$

In our specific case, the pretension term  $T/L$  can be ignored for three reasons. First, according to previous



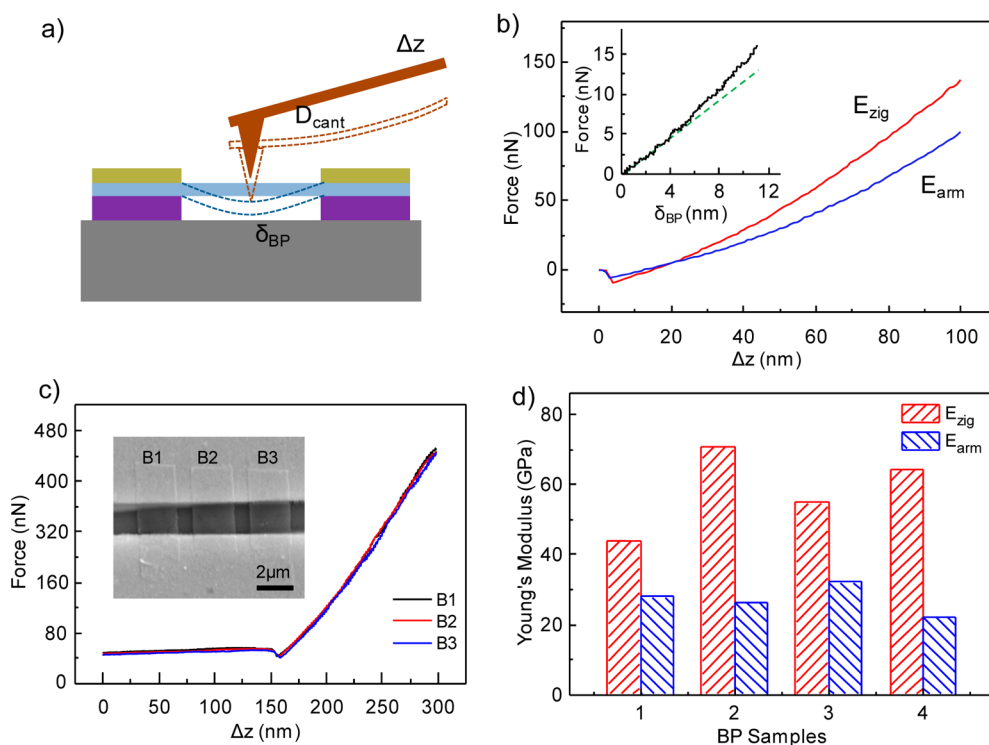


**Figure 4.** Young's modulus measurements. (a) Schematic diagram of the AFM bending measurement carried out on the suspended BP strip. (b) Load force vs displacement curves of the AFM tip taken on the armchair and zigzag strips, respectively. The inset shows the relationship between the AFM load force and the deformation of the BP strip. The curve is almost linear below 5 nm and becomes nonlinear at larger displacement due to film stretching. (c) Repeatability test of the AFM bending method carried out on three suspended strips with the same size and lattice orientation and trimmed from the same BP flake. (d) Young's modulus in the zigzag and the armchair directions of four pairs of suspended BP strips.  $E_{\text{zig}}$  is on average about 2.2 times higher than  $E_{\text{arm}}$  ( $E_{\text{zig}} = 58.6 \pm 11.7$  GPa,  $E_{\text{arm}} = 27.2 \pm 4.1$  GPa).

reports, the pretension will affect the spring constant by less than  $\sim 15\%$  in monolayer graphene and few-layer  $\text{MoS}_2$  thin films.<sup>14,15,17,18</sup> The BP flakes in our study are substantially thicker; therefore the pretension has a minimal effect. Second, the BP flakes were trimmed into strips by  $\text{Ar}^+$  plasma, which largely released the tension inside the 2D crystal. Third, the suspended structures were created by sacrificial layer release, which was supposed to induce much less tensional stress compared to the approach of transferring 2D films onto pre-etched trenches.<sup>14</sup>

In this study, we obtained the stiffness of the BP beams by linear fitting the first 5 nm of the force curves (Figure 4b inset). The measured stiffness was then taken into eq 3 (ignoring the pretension term) to calculate the Young's modulus.

The test in Figure 4c was to evaluate the consistency of the AFM bending method. We fabricated three BP strips with identical geometry and lattice orientation (Figure 4c inset) and recorded the force curve on each strip separately. The three curves were in perfect accordance with each other, indicating excellent consistency and repeatability of the measurement. The data also suggested fairly small device-to-device variation resulted from our optimized fabrication processes. We can therefore safely attribute the difference in force curves to the intrinsic anisotropy of BP.

We performed Young's modulus measurements on four pairs of BP strips and summarized the data in Figure 4d. The results revealed a sharp contrast between the elasticity along the armchair and zigzag directions. The Young's moduli of the "armchair strips" (identified by the electron transport characterizations) are collectively lower than those of "zigzag strips" by a factor of 1.6 to 2.9. We note that since each pair of strips was trimmed from the same BP flake, differences in film thickness and material qualities (*e.g.*, disorders and impurities) were quite minimal and made negligible contribution to the anisotropic results. However, different thickness and material qualities among different BP flakes were likely the major cause of the observed device-to-device variations.

The average Young's moduli in armchair and zigzag directions,  $E_{\text{arm}}$  and  $E_{\text{zig}}$ , were calculated to be  $27.2 \pm 4.1$  and  $58.6 \pm 11.7$  GPa, respectively, according to our experimental results. The numbers are in very good agreement with the theoretical predictions both qualitatively and quantitatively.<sup>29–31</sup> The elastic anisotropy of few-layer BP can be explained by its puckered crystal structure. Specifically, the "atomic puckers" along the zigzag direction can relatively easily comply with the stretching by a tensional stress along the armchair direction. The anisotropic atomic structure has therefore resulted in a much lower Young's

modulus in the armchair direction. We also noted that the measured Young's moduli in both directions were significantly smaller compared to the values of graphene<sup>14,15</sup> and MoS<sub>2</sub>.<sup>17,18</sup>

We did not observe a clear thickness-dependence pattern among that 20 samples (15–25 nm) we have measured. In general, the Young's modulus of 2D materials decreases monotonically with thickness due to defects and/or interlayer sliding.<sup>18</sup> The changes are most pronounced between single and double layers (14.6% for BP<sup>30</sup> and 29.8% for MoS<sub>2</sub><sup>18</sup>) and become less sensitive in thicker materials. Wei *et al.* stated that the Young's moduli were fairly similar between double-layer, three-layer, and bulk BP (when compared in the same lattice orientation) due to negligible interlayer interactions.<sup>30</sup> We experienced from material stability issues and failed to reliably process and characterize samples below 10 nm. Nonetheless, we believe our experimental results also resemble the behavior of ultrathin films to a considerable extent.

**Breaking Stress and Strain.** Besides the Young's modulus, the AFM bending method can also measure the breaking stress and strain by continually increasing the loading force until the beam is broken.<sup>14,18</sup> Breaking stress and strain characterize the strength and flexibility of the BP strips, respectively. Figure 5a shows the curve of loading force vs displacement of the AFM cantilever. The sudden drop in the curve corresponds

to the breaking of the BP strip. The inset is the AFM image of the broken strip. A pinhole can be seen near the center of the strip, as indicated by the arrow.

It is worth noting that a much stiffer AFM cantilever ( $k_{\text{cant}} > 15$  N/m) has to be used to break the suspended BP beams at such large deformation and load force. In our study, we chose a cantilever with the effective spring constant of 34.9 N/m as calibrated before the measurement.

To extract the maximum stress at the broken point, we used the same model that had been previously developed for graphene and MoS<sub>2</sub> for approximate calculation.<sup>14,18</sup> The maximum stress  $\sigma_{\text{max}}^{2\text{D}}$  can be derived by

$$\sigma_{\text{max}}^{2\text{D}} = \sqrt{\frac{F_{\text{max}} E^{2\text{D}}}{4\pi r_{\text{tip}}}} \quad (6)$$

$F_{\text{max}}$  is the breaking force,  $E^{2\text{D}}$  is the 2D elastic constant, which can be derived by multiplying the bulk Young's modulus by the thickness ( $E^{3\text{D}} \times t$ ), and  $r_{\text{tip}}$  is the radius of the AFM tip. The breaking force depends strongly on  $r_{\text{tip}}$  instead of the sample size.

We measured four pairs of BP strips with different thickness and sizes. The breaking forces of the zigzag strips are consistently larger than the armchair ones, as shown in Figure 5b. The average breaking force in the zigzag direction ( $\sim 2.44$   $\mu\text{N}$ ) is 1.74 times that of the armchair direction ( $\sim 1.40$   $\mu\text{N}$ ). The breaking stress

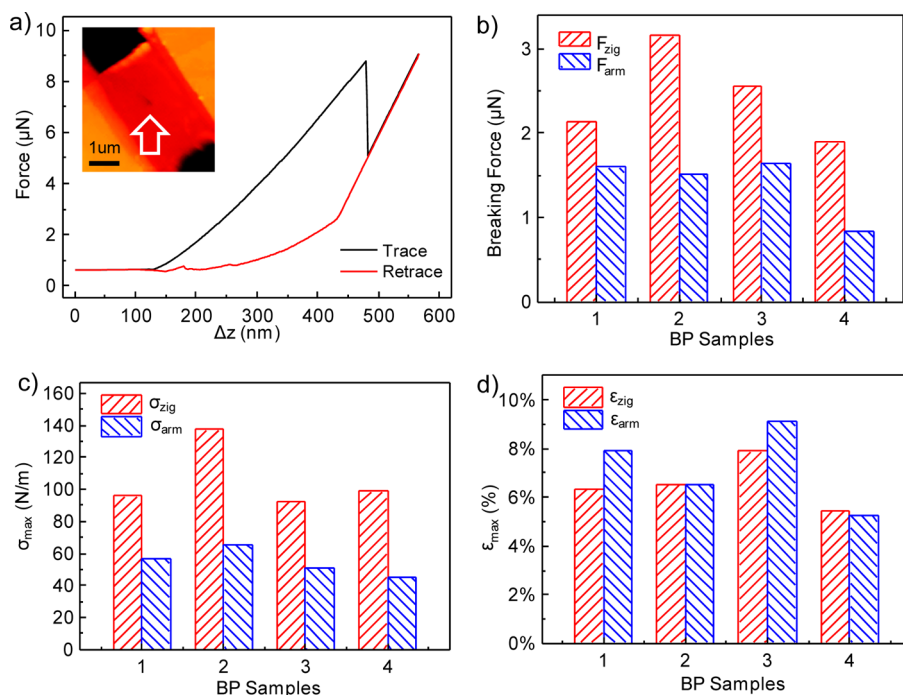


**Figure 5.** Breaking stress and strain measurements. (a) Load force vs displacement of the AFM tip. A sudden drop in the trace curve indicates the breaking of the BP strip. The inset AFM image shows the break point near the center of the strip. (b) Histogram showing the maximum breaking forces of four pairs of orthogonal suspended strips. (c) Breaking stress of the same samples in (b). The average breaking stress,  $\sigma_{\text{max}}$ , in the zigzag direction (106.2 N/m) is about 1.94 times that in the armchair direction (54.8 N/m), a ratio very close to that of the anisotropic Young's modulus. (d) Breaking strain of the same samples in (b). The breaking strain exhibited a relatively small difference in the two lattice axes, ranging from 5.3% to 9.2% in different samples.

calculated by eq 5 is 106.2 N/m (4.22 GPa) and 54.8 N/m (2.21 GPa) in the zigzag and armchair direction, respectively (Figure 5c). The results indicate that the strength of BP is highly anisotropic, which primarily results from the anisotropic Young's modulus along the armchair and zigzag directions.

Breaking strain is calculated by assuming a linear relationship between stress and strain,  $\sigma = E\varepsilon$ . The result is shown in Figure 5d. The average strain is 6.5% and 7.2% in the zigzag and armchair directions, respectively. The two numbers are rather close, as the anisotropic breaking stress and Young's modulus largely offset each other. The flexibility of BP is comparable to most polymeric substrates commonly used for flexible electronics such as polyimide and polydimethylsiloxane.<sup>46</sup> Few-layer BP can therefore be readily integrated into flexible circuits as functional electronic and/or electromechanical elements. The maximum breaking strain measured in our experiments was 9.2%, considerably close to the theoretical upper limit of the breaking strength ( $E/9$ ),<sup>47</sup> indicating very low density of disorders and impurities in the BP crystals.

## MATERIALS AND METHODS

**Suspended BP Strip Fabrication.** Few-layer BP flakes were mechanically exfoliated from BP crystals (Smart Elements) and transferred onto a silicon substrate with a 200 nm thick thermal oxide layer. The flakes were trimmed into orthogonal strips along the principal lattice axes by  $\text{Ar}^+$  plasma (recipe:  $\text{Ar}$  flow  $\sim 80$  sccm, pressure  $\sim 20$  Pa, RF power  $\sim 80$  W). Metal anchors/electrodes were deposited at the ends of each strip through e-beam evaporation followed by a lift-off process to hold the strips upon sacrificial layer removal and form electrical connections to external test circuits. Finally, the thermal oxide layer was removed by BOE to release and suspend the BP strips. EBL (SEM: FEI; EBL: Raith; e-beam resist: Allresist AR-P679.04) was used for patterning in the  $\text{Ar}^+$  plasma trimming and metal anchor deposition processes.

**AFM Measurement.** A Dimension Icon (Bruker) AFM was used for this study. The AFM worked in tapping mode and force curve mode for the imaging and bending test, respectively. An RFESP-MPP21100 (Bruker) cantilever was applied for the Young's modulus measurement. An RTESP-MPP-11100 cantilever was applied for the breaking stress measurement. The nominal spring constants of these two cantilevers are 3 and 40 N/m, respectively. For such stiff cantilevers, the standard thermotune method is inaccurate for the spring constant calibration. Thus, we used a homemade calibration system based on static bending to precisely determine the effective spring constant of these cantilevers. The spring constant calibration was performed before the measurement of BP beams. The calibrated spring constants of these two cantilevers are  $3.429 \pm 0.041$  and  $34.901 \pm 0.425$  N/m, respectively. Since the tip radius is significant to the calculation of breaking stress, we also calibrated the shape of the tip experimentally. This calibration was realized by scanning the tip over a tip-check sample (produced by Bruker) after the bending test, and then the profile of the tip was extracted from the image by using a commercial software based on the blind-tip-reconstruction algorithm.<sup>48</sup> The radius of the tip was estimated to be 28 nm according to the calibration.

**Conflict of Interest:** The authors declare no competing financial interest.

**Acknowledgment.** We thank Prof. Dong Sun from Peking University for valuable discussions. This work was financially

## CONCLUSIONS

We combined RDM characterization and electron transport measurements to successfully identify the lattice orientation of individual BP flakes. This enabled us to characterize the mechanical and electrical behaviors along different lattice axes on separate devices. The mechanical anisotropy of few-layer BP was systematically investigated by nanoindentation in AFM, and the anisotropic transport properties were evaluated through  $I$ – $V$  measurements under various gate biases. We obtained the anisotropic ratio of the Young's moduli, breaking strain, and dc conductance between the armchair and zigzag directions to be 2.2, 1.94, and 1.93, respectively. In addition, the maximum breaking strain measured in our experiment ( $\varepsilon_{\text{max}} = 9.2\%$ ) was fairly close to the theoretical upper limit of 2D materials, indicating good structural quality of the BP crystal. The unique mechanical and electrical properties of BP make it a promising material for applications in flexible electronics, strain-dependent optoelectronics, and electromechanical nanodevices.

supported by the 111 Project (B07014). D.Z. acknowledges support by the Tianjin Applied Basic Research and Advanced Technology (13JYBJC37100).

## REFERENCES AND NOTES

- Martiradonna, L. Black Phosphorus: Undercover Operation. *Nat. Mater.* **2014**, *14*, 13.
- Reich, E. S. Phosphorene Excites Materials Scientists. *Nature* **2014**, *506*, 19.
- Ling, X.; Wang, H.; Huang, S.; Xia, F.; Dresselhaus, M. S. The renaissance of black phosphorus. *Proc. Natl. Acad. Sci. U. S. A.* **2015**, *112*, 4523–4530.
- Li, L.; Yu, Y.; Ye, G. J.; Ge, Q.; Ou, X.; Wu, H.; Feng, D.; Chen, X. H.; Zhang, Y. Black Phosphorus Field-Effect Transistors. *Nat. Nanotechnol.* **2014**, *9*, 372–377.
- Xia, F.; Wang, H.; Jia, Y. Rediscovering Black Phosphorus as an Anisotropic Layered Material for Optoelectronics and Electronics. *Nat. Commun.* **2014**, *5*, 4458.
- Liu, H.; Neal, A. T.; Zhu, Z.; Luo, Z.; Xu, X.; Tománek, D.; Ye, P. D. Phosphorene: An Unexplored 2D Semiconductor with a High Hole Mobility. *ACS Nano* **2014**, *8*, 4033–4041.
- Liu, H.; Du, Y.; Deng, Y.; Ye, P. D. Semiconducting Black Phosphorus: Synthesis, Transport Properties and Electronic Applications. *Chem. Soc. Rev.* **2015**, *44*, 2732–2743.
- Doganov, R. A.; Koenig, S. P.; Yeo, Y.; Watanabe, K.; Taniguchi, T. Transport Properties of Ultrathin Black Phosphorus on Hexagonal Boron Nitride Transport Properties of Ultrathin Black Phosphorus on Hexagonal Boron Nitride. *Appl. Phys. Lett.* **2015**, *106*, 083505.
- Koenig, S. P.; Doganov, R. A.; Schmidt, H.; Castro Neto, A. H.; Özyilmaz, B. Electric Field Effect in Ultrathin Black Phosphorus. *Appl. Phys. Lett.* **2014**, *104*, 103106.
- Low, T.; Rodin, A. S.; Carvalho, A.; Jiang, Y.; Wang, H.; Xia, F.; Neto, A. H. C. Tunable Optical Properties of Multilayers Black Phosphorus. *arXiv* **2014**, 075434, 1–5.
- Buscema, M.; Groenendijk, D. J.; Blanter, S. I.; Steele, G. A.; Van Der Zant, H. S. J.; Castellanos-Gomez, A. Fast and Broadband Photoresponse of Few-Layer Black Phosphorus Field-Effect Transistors. *Nano Lett.* **2014**, *14*, 3347–3352.



12. Hong, T.; Chamlagain, B.; Lin, W.; Chuang, H.-J.; Pan, M.; Zhou, Z.; Xu, Y.-Q. Polarized Photocurrent Response in Black Phosphorus Field-Effect Transistors. *Nanoscale* **2014**, *6*, 8978–8983.
13. Yuan, H.; Liu, X.; Afshinmanesh, F.; Li, W.; Xu, G.; Sun, J.; Lian, B.; Curto, A. G.; Ye, G.; Hikita, Y.; et al. Polarization-Sensitive Broadband Photodetector Using a Black Phosphorus Vertical p–n Junction. *Nat. Nanotechnol.* **2015**, *10*, 707–713.
14. Lee, C.; Wei, X.; Kysar, J. W.; Hone, J. Measurement of the Elastic Properties and Intrinsic Strength of Monolayer Graphene. *Science* **2008**, *321*, 385–388.
15. Frank, I. W.; Tanenbaum, D. M.; van der Zande, a. M.; McEuen, P. L. Mechanical Properties of Suspended Graphene Sheets. *J. Vac. Sci. Technol. B Microelectron. Nanom. Struct.* **2007**, *25*, 2558.
16. Ong, M. T.; Reed, E. J. Engineered Piezoelectricity in Graphene. *ACS Nano* **2012**, *6*, 1387–1394.
17. Castellanos-Gomez, A.; Poot, M.; Steele, G. a.; Van Der Zant, H. S. J.; Agraït, N.; Rubio-Bollinger, G. Elastic Properties of Freely Suspended MoS<sub>2</sub> Nanosheets. *Adv. Mater.* **2012**, *24*, 772–775.
18. Bertolazzi, S.; Brivio, J.; Kis, A. Stretching and Breaking of Ultrathin MoS<sub>2</sub>. *ACS Nano* **2011**, *5*, 9703–9709.
19. Wu, W.; Wang, L.; Li, Y.; Zhang, F.; Lin, L.; Niu, S.; Chenet, D.; Zhang, X.; Hao, Y.; Heinz, T. F.; et al. Piezoelectricity of Single-Atomic-Layer MoS<sub>2</sub> for Energy Conversion and Piezotronics. *Nature* **2014**, *514*, 470–474.
20. Manzeli, S.; Allain, A.; Ghadimi, A.; Kis, A. Piezoresistivity and Strain-Induced Band Gap Tuning in Atomically Thin MoS<sub>2</sub>. *Nano Lett.* **2015**, *15*, 5330–5335.
21. Zhu, W.; Yogeesh, M. N.; Yang, S.; Aldave, S. H.; Kim, J.; Sonde, S. S.; Tao, L.; Lu, N.; Akinwande, D. Flexible Black Phosphorus Ambipolar Transistors, Circuits and AM Demodulator. *Nano Lett.* **2015**, *15*, 1883–1990.
22. Wang, Y.; Yang, R.; Shi, Z.; Zhang, L.; Shi, D.; Wang, E.; Zhang, G. Super-Elastic Graphene Ripples for Flexible Strain Sensors. *ACS Nano* **2011**, *5*, 3645–3650.
23. Wang, Z. Z.; Jia, H.; Zheng, X.; Yang, R.; Wang, Z. Z.; Ye, G. J.; Chen, X. H.; Shan, J.; Feng, P. X.-L. Black Phosphorus Nanoelectromechanical Resonators Vibrating at Very High Frequencies. *Nanoscale* **2015**, *7*, 877–884.
24. Li, Y.; Yang, S.; Li, J. The Modulation of the Electronic Properties of Ultrathin Black Phosphorus by Strain and Electrical Field. *J. Phys. Chem. C* **2014**, *118*, 23970–23976.
25. Rodin, A. S.; Carvalho, A.; Castro Neto, A. H. Strain-Induced Gap Modification in Black Phosphorus. *Phys. Rev. Lett.* **2014**, *112*, 1–5.
26. Han, X.; Morgan Stewart, H.; Shevlin, S. A.; Catlow, C. R. A.; Guo, Z. X. Strain and Orientation Modulated Bandgaps and Effective Masses of Phosphorene Nanoribbons. *Nano Lett.* **2014**, *14*, 4607–4614.
27. Fei, R.; Yang, L. Strain-Engineering the Anisotropic Electrical Conductance of Few-Layer Black Phosphorus. *Nano Lett.* **2014**, *14*, 2884–2889.
28. Jiang, J.-W.; Park, H. S. Negative Poisson's Ratio in Single-Layer Black Phosphorus. *Nat. Commun.* **2014**, *5*, 1–7.
29. Yang, Z.; Zhao, J.; Wei, N. Temperature-Dependent Mechanical Properties of Monolayer Black Phosphorus by Molecular Dynamics Simulations. *Appl. Phys. Lett.* **2015**, *107*, 023107.
30. Wei, Q.; Peng, X. Superior Mechanical Flexibility of Phosphorene and Few-Layer Black Phosphorus. *Appl. Phys. Lett.* **2014**, *104*, 251915.
31. Jiang, J.; Park, H. S. Mechanical Properties of Single-Layer Black Phosphorus. *J. Phys. D: Appl. Phys.* **2014**, *47*, 385304.
32. Hu, C.; Xie, P.; Huo, S.; Li, Y.; Hu, X. A Liquid Crystal Variable Retarder-Based Reflectance Difference Spectrometer for Fast, High Precision Spectroscopic Measurements. *Thin Solid Films* **2014**, *571*, 543–547.
33. Hu, C. G.; Sun, L. D.; Flores-Camacho, J. M.; Hohage, M.; Liu, C. Y.; Hu, X. T.; Zeppenfeld, P. A Rotating-Compensator Based Reflectance Difference Spectrometer for Fast Spectroscopic Measurements. *Rev. Sci. Instrum.* **2010**, *81*, 043108.
34. Weightman, P.; Martin, D. S.; Cole, R. J.; Farrell, T. Reflection Anisotropy Spectroscopy. *Rep. Prog. Phys.* **2005**, *68*, 1251.
35. Castellanos-Gomez, A.; Vicarelli, L.; Prada, E.; Island, J. O.; Narasimha-Acharya, K. L.; Blanter, S. I.; Groenendijk, D. J.; Buscema, M.; Steele, G. a.; Alvarez, J. V.; et al. Isolation and Characterization of Few-Layer Black Phosphorus. *2D Mater.* **2014**, *1*, 025001.
36. Wood, J. D.; Wells, S. A.; Jariwala, D.; Chen, K.-S.; Cho, E.; Sangwan, V. K.; Liu, X.; Lauhon, L. J.; Marks, T. J.; Hersam, M. C. Effective Passivation of Exfoliated Black Phosphorus Transistors against Ambient Degradation. *Nano Lett.* **2014**, *14*, 6964–6970.
37. Island, J. O.; Steele, G. A.; Van Der Zant, H. S. J.; Castellanos-gomez, A. Environmental Instability of Few-Layer Black Phosphorus. *2D Mater.* **2015**, *2*, 11002.
38. Asahina, H.; Morita, a. Band Structure and Optical Properties of Black Phosphorus. *J. Phys. C: Solid State Phys.* **1984**, *17*, 1839–1852.
39. Tran, V.; Soklaski, R.; Liang, Y.; Yang, L. Layer-Controlled Band Gap and Anisotropic Excitons in Few-Layer Black Phosphorus. *Phys. Rev. B: Condens. Matter Mater. Phys.* **2014**, *89*, 1–6.
40. Tombros, N.; Veligura, A.; Junesch, J.; Jasper Van Den Berg, J.; Zomer, P. J.; Wojtaszek, M.; Vera Marun, I. J.; Jonkman, H. T.; Van Wees, B. J. Large Yield Production of High Mobility Freely Suspended Graphene Electronic Devices on a Polydimethylglutarimide Based Organic Polymer. *J. Appl. Phys.* **2011**, *109*, 14.
41. Bolotin, K. I.; Sikes, K. J.; Jiang, Z.; Klima, M.; Fudenberg, G.; Hone, J.; Kim, P.; Stormer, H. L. Ultrahigh Electron Mobility in Suspended Graphene. *Solid State Commun.* **2008**, *146*, 351–355.
42. Qiao, J.; Kong, X.; Hu, Z.-X.; Yang, F.; Ji, W. High-Mobility Transport Anisotropy and Linear Dichroism in Few-Layer Black Phosphorus. *Nat. Commun.* **2014**, *5*, 4475.
43. Pruessner, M. W.; King, T. T.; Kelly, D. P.; Grover, R.; Calhoun, L. C.; Ghodssi, R. Mechanical Property Measurement of InP-Based MEMS for Optical Communications. *Sens. Actuators, A* **2003**, *105*, 190–200.
44. Song, Y.-P.; Wu, S.; Xu, L.-Y.; Zhang, J.-M.; Dorantes-Gonzalez, D. J.; Fu, X.; Hu, X.-D. Calibration of the Effective Spring Constant of Ultra-Short Cantilevers for a High-Speed Atomic Force Microscope. *Meas. Sci. Technol.* **2015**, *26*, 065001.
45. Timoshenko, S.; Woinowsky-Krieger, S. *Theory of Plates and Shells*; McGraw-Hill: New York, 1959.
46. Kim, D.-H.; Ahn, J.-H.; Choi, W. M.; Kim, H.-S.; Kim, T.-H.; Song, J.; Huang, Y. Y.; Liu, Z.; Lu, C.; Rogers, J. a. Stretchable and Foldable Silicon Integrated Circuits. *Science* **2008**, *320*, 507–511.
47. Griffith, A. A. The Phenomena of Rupture and Flow in Solids. *Philos. Trans. R. Soc., A* **1921**, *221*, 163–198.
48. Dongmo, L. S.; Villarrubia, J. S.; Jones, S. N.; Renegar, T. B.; Postek, M. T.; Song, J. F. Experimental Test of Blind Tip Reconstruction for Scanning Probe Microscopy. *Ultramicroscopy* **2000**, *85*, 141–153.